Chapter 12
Effects of Hyperfine Interaction in Atomic Photoionization

Elena V. Gryzlova and Alexei N. Grum-Grzhimailo

Abstract The chapter is devoted to theoretical consideration of the role of hyperfine interaction in atomic photoionization. The interaction between nuclear spin and an atomic shell considered to give a small correction in a variety of phenomena may have significant effects on polarization and correlation parameters of a process. We outline a theoretical approach based on statistical tensors and density matrices for determination of photoelectron angular distribution in two-colour atomic ionization accounting for their evolution caused by nuclear spin. As a practical example we consider double resonant ionization of Xe through excitation via discrete and Rydberg autoionizing states, as in the first isotope-selective experiment in VUV domain (O'Keeffe et al in Phys Rev Lett 111:243002(1)–243002(5), 2013 [44]). Variations in the angular pattern for the different isotopes and light polarization are shown. The possibility to determine the hyperfine constant is discussed.

12.1 Introduction

One of the commonest and widely used technique in quantum mechanics, starting from Born-Oppenheimer approximation in molecular physics [9] up to single-particle shell model [23] in nuclear physics is the separation of degrees of freedom. In atomic physics scientists commonly separate nuclear and atomic-shell parameters by treating their interaction as a hyperfine correction.

Even though the hyperfine interaction is widely considered to have only a small effect or correction, it is crucially important for understanding of the interplay between atomic and nuclear degrees of freedom as well as for many applications. The transition between hyperfine structure (HFS) levels of the ground state of a hydrogen atom produces famous 21 cm radiation (Fig. 12.1) which is used for imaging

E. V. Gryzlova (✉) · A. N. Grum-Grzhimailo
Skobeltsyn Institute of Nuclear Physics, Lomonosov Moscow State University, Moscow 119991, Russia
e-mail: gryzlova@gmail.com

A. N. Grum-Grzhimailo
e-mail: grum@sinp.msu.ru

K. Yamanouchi et al. (eds.), *Progress in Photon Science*, Springer Series in Chemical Physics 119, https://doi.org/10.1007/978-3-030-05974-3_12

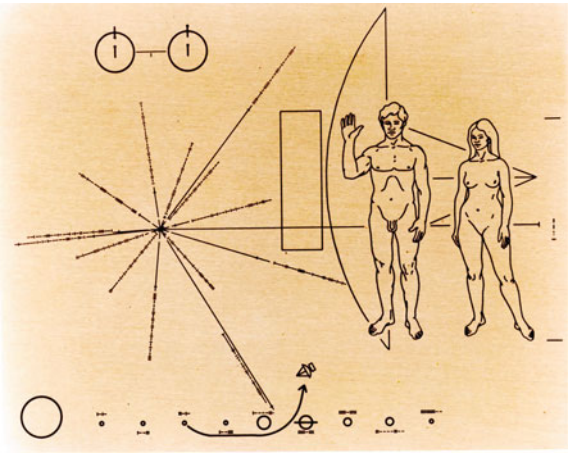

Fig. 12.1 The Pioneer plaques: a gold-anodized aluminium plaques which were placed on board the 1972 Pioneer 10 and 1973 Pioneer 11 spacecraft, featuring a pictorial message, to be intercepted by extraterrestrial life. The scaling is based on the hyperfine transition of a hydrogen atom whose wavelength is 21 cm

galaxies [10, 31, 39] and for serving as a metric to distance determination. Pumping of HFS levels is of importance in generation of coherent radiation starting from the first maser [47] to X-ray lasers [48]. The hyperfine interaction affects polarization of spectral lines used in plasma diagnostics [30]; it may change a forbidden transition to an allowed one [51, 55], or change the transition type [14], sometimes drastically decreasing life-time of an excited state [7, 52]. The atomic clocks are based on transitions between the HFS levels since the early beginning [16] and up to now [11, 21, 58]. Investigations of hyperfine interaction are actively developing because of possible implementation to quantum entanglement and quantum computations.

If an atomic nucleus possesses a nonzero spin, I, the interaction of the total angular momentum of the electronic shell, J, with the magnetic field created by the atomic nucleus leads to the hyperfine splitting. The HFS level is described by the state vector $|\,(JI)FM_F\,\rangle$, where F, M_F denote the total angular momentum of atom and its projection, respectively. Each F-sublevel evolves with a frequency corresponding to complex quasienergy $E_F - i\Gamma_F/2$, where the real part corresponds to the energy and the imaginary part describes the width of the HFS level. The density matrix of the electron-shell momentum J, $\rho_{JM,J'M'} \equiv \langle JM \mid \rho \mid J'M'\rangle$, is defined according to the standard prescriptions by a trace of the density matrix of the total atomic angular momentum, $\rho_{FM_F,F'M_{f'}} \equiv \langle (JI)FM_F \mid \rho \mid (JI)F'M_{F'}\rangle$, over the quantum numbers of the unobserved subsystem, i.e., the atomic nucleus. We consider here an isotope with a nuclear spin $\boldsymbol{I}$. The decoupling of $\boldsymbol{F}$ and $\boldsymbol{J}$ leads to

$$\rho_{JM,J'M'} = \sum_{FF'M_FM'_FM_I} (JM_J, IM_I \mid FM_F)\left(J'M'_J, IM_I \mid F'M'_F\right)\rho_{FM_F,F'M'_F}\,, \quad (12.1)$$

where the Clebsch-Gordan coefficients are introduced. The diagonal density matrix elements evolve as $\rho_{FM_F,FM_F} \sim \exp(-\Gamma_F t)$, decaying with time, while the non-diagonal elements evolve as $\rho_{FM_F,F'M'_F} \sim \exp\left(i\omega_{FF'}t - \frac{1}{2}(\Gamma_F + \Gamma'_F)t\right)$, decaying and oscillating with time. Then each element of the density matrix of the electronic

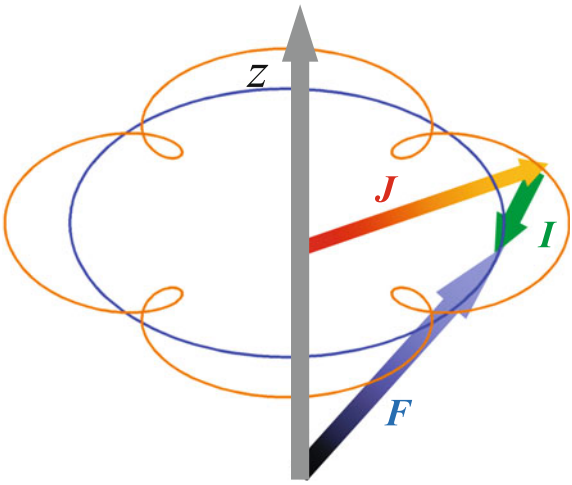

Fig. 12.2 Classical interpretation of hyperfine interaction. Projection M_F of the total angular momentum is a well-defined quantum number, presented as the cone or rotation of $\boldsymbol{F}$ around the quantization axis (gray arrow). At any moment $\boldsymbol{F}=\boldsymbol{J}+\boldsymbol{I}$, but neither M_J or M_I is well-defined and measurements at different times give different values for M_J and M_I. (See text for notations)

shell (12.1) oscillates with the number of frequencies, $\omega_{FF'} = E_F - E_{F'}$ defined by the energy splittings[1] of the HFS levels.

When HFS levels of an atom are coherently excited, a beating in electronic shell arises as result of the precession of the total angular momentum of the electronic shell in magnetic field created by the atomic nucleus (Fig. 12.2). A typical evolution of the density matrix elements of the electronic shell is shown in Fig. 12.3. The effect is similar to the zero-field beating observed due to coherent excitation of different magnetic sublevels split by an external magnetic field (Zeeman effect), and has been known since the middle of 1960s. Alexandrov and Kulyasov [1] and Hadeishi and Nierenberg [28] observed modulation of the fluorescence from atoms excited by electron impact. Alexandrov and his colleagues also observed modification of spectral profiles of the fluorescence lines after the excitation using optical laser [2, 3]. Resolving the time modulation of the fluorescence after photoexcitation was a much more demanding experimental task and the first experiment was performed later by Haroch, Paisne and Shawlow [29], two of them becoming later the Nobel laureates (Shawlow in 1981; Haroch in 2012). Investigations of the quantum beats were further stimulated by the development of time- and angular-resolved photoelectron spectroscopy after the measurements of the photoelectron angular distributions in two-photon resonant ionization became possible. In a series of papers by Berry with coauthors, a general approach for description of the quantum beats was formulated in terms of statistical tensor formalism and applied to lithium and alkaline earth metals [12, 40]. The applications finally became so numerous and various that the new types of spectroscopy were developed into a broad research field named "quantum beat spectroscopy" [27, 53].

The relative population evolution of magnetic substates $| J M_J \rangle$ is the evolution of the polarization of the atomic state with the total angular momentum of the electronic

[1] Atomic units are used hereafter $\hbar = e = m_e = 1$, unless otherwise specified.

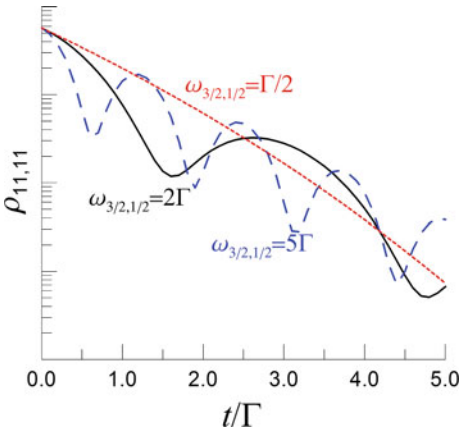

Fig. 12.3 The evolution of (unnormalized) density matrix element $\rho_{11,11}$ of the electronic shell, corresponding to the population of state with $J = 1$, $M = 1$ of a model atom with nuclear spin $I = 1/2$. The value $\omega_{3/2,1/2} = E_{3/2} - E_{1/2}$ is the energy splitting between HFS levels $F = 3/2$ and $F' = 1/2$. It is assumed that $\Gamma_{3/2} = \Gamma_{1/2} = \Gamma$

shell $\boldsymbol{J}$. To characterize this polarization and to obtain observable quantities, such as photoelectron angular distributions, the density matrix and statistical tensor (state multipole) technique is applied [6, 8]. The statistical tensor of the angular momentum J (which can take different values) is related to the density matrix of this momentum as

$$\rho_{kq}(J, J') = \sum_{MM'} (-1)^{J'-M'} \left(JM, J' - M' \,|\, kq\right) \rho_{JM,J'M'}\,, \tag{12.2}$$

where $k = |J - J'|,\ |J - J'| + 1,\ \ldots,\ J + J' - 1,\ J + J'$ and $-k \le q \le k$. For isotropic system only zero-rank tensor (12.2) ($k = q = 0$) is non-vanishing. The angular momentum is polarized when at least one of the statistical tensors with $k \neq 0$ is nonzero.

Polarization of an atomic state can be produced by different means. One of the methods is optical excitation, for example, by laser. The advantage of this method is that polarization of optical and IR lasers is easy to control. Excitation of an atom by light with definite polarization produces aligned or oriented state: in the dipole approximation linearly polarized radiation excites an atom from a state with $J = 0$ to the magnetic substate with $J = 1$, $M = 0$ (quantization axis along the electric vector of the radiation) and right(left) polarized radiation excites the same state to the substate $J = 1$, $M = +1$ ($J = 1$, $M = -1$) (quantization axis along the radiation beam).

Polarization of an atomic state may manifest itself, sometimes crucially, in different ways, for example, in the complicated angle dependence of electron emission and fluorescence, generated by the higher rank ($k > 2$) statistical tensors (12.2) [43, 56], or in the modification of ionization probability and creation of inverse population [57]. The quantum beats decrease the effect of the polarization (12.2) as time goes on and can make the polarization disappear, on which a good overview can be found in [18]. An interesting graphical approach was applied in [33, 35] to analysis of the hyperfine quantum beats. It should be mentioned that depolarization occurs

due to the collisions in the reaction volume and the radiation trapping in addition to the HFS-caused depolarization. The former will not be discussed here: although their influence may be strong [15, 37, 49], it will not be the case in the experiments discussed below [44, 46].

Evolution of atomic polarization due to HFS can be determined in experiments with two conjugate polarizations, for instance, in experiment on circular magnetic dichroism [13, 20, 45]. The hyperfine interactions play a crucial role in realization of different schemes of optical pumping [19, 36, 42]. The development of synchrotron and free-electron laser facilities, producing brilliant XUV radiation, allows us to change typical targets in the experimental studies on the effects of the hyperfine interaction on the atomic processes from alkali and alkali earth elements to noble gases. Experimental techniques are progressing, and recently, even the direct observation of the quantum beats in this energy domain became feasible [22].

Natural mixtures of isotopes for neon and argon are dominated by the isotopes with zero nuclear spin, which do not generate the hyperfine splitting. Xenon containing nine stable isotopes with the nuclear spins $I = 0,\ 1/2,\ 3/2$ with the corresponding abundance ratios $53 : 26 : 21$ is an appropriate target for the studies described below. Conventional experiments on measurements of the photoelectron angular distributions in resonant ionization were performed with the Xe isotopes with the natural abundance ratios [4, 38, 54]. The first measurements of photoelectron angular distributions for the selected isotopes [44] were performed at the French synchrotron SOLEIL. The first VUV photon excited $Xe^*(5p^5\,{}^2P_{3/2})5d[3/2]_1$ state,[2] and then, a photon from the optical laser excited it into the $Xe^{**}(5p^5\,{}^2P_{1/2})4f[5/2]_2$ Rydberg autoionizing state, which subsequently decays with emission of an electron. The key point is that these emitted electrons were detected in coincidence with a mass-selected ion from which its spin ($I = 0$, $I = 1/2$, or $I = 3/2$) can be specified. The experiment was done using the photon beams with various polarizations. The analysis of the experiment was given in [26]. Later, a similar joint experimental and theoretical investigation was performed using Kr [46] for the sequence of discrete states $[^2P_{3/2}]4d[1/2]_1$, $[^2P_{3/2}]5d[1/2]_1$, $[^2P_{1/2}]4d[3/2]_1$, $[^2P_{3/2}]5d[3/2]_1$, $[^2P_{1/2}]6s[1/2]_1$ with the natural isotope mixture containing 11.5% of the isotope with $I = 9/2$.

12.2 Formal Description

We are going to present here detailed description of our method on a practical example of two-photon resonant ionization of xenon. The method has also been applied to krypton [46] and can be applied to any initially unpolarized atoms or ions. The

[2] In the jK-coupling scheme, the $nl[K]_J$ indicates, for the Xe atom, that the total angular momentum j of the $5p_j^5$ core is first coupled to the orbital momentum of the excited electron $\boldsymbol{\ell}$, $\boldsymbol{j} + \boldsymbol{\ell} = \boldsymbol{K}$, with subsequent coupling of spin of this electron, $\boldsymbol{K} + \boldsymbol{s} = \boldsymbol{J}$.

theoretical approach is based on the formalism of the statistical tensors and the polarization density matrix [6, 8].

In the first step, the atom is excited by a photon with ω_1

$$\omega_1 \; + \; \mathrm{Xe}\,(5p^6) \rightarrow \mathrm{Xe}^*(5p^{5\,2}P_{3/2})5d[3/2]_1\,. \tag{12.3}$$

Initially unpolarized atoms with the total angular momentum J_0 (here $J_0 = 0$) become polarized after excitation into the intermediate state Xe* with the electron-shell angular momentum J_i (here $J_i = 1$). The excited atom is further excited by the photon ω_2, followed by the autoionizing decay and emission of a photoelectron,

$$\begin{aligned} \omega_2 \; + \mathrm{Xe}^*(5p^{5\,2}P_{3/2})5d[3/2]_1 &\rightarrow \mathrm{Xe}^{**}(5p^{5\,2}P_{1/2})4f[5/2]_2\,, \\ &\rightarrow \mathrm{Xe}^+\,(5p^{5\,2}P_{3/2}) + e^-(\ell j)\,. \end{aligned} \tag{12.4}$$

We emphasize that the method is applicable either with or without autoionizing states at the second step, but it is important that the final state is described in the representation $|\,(L_f S_f)J_f;\,\ell j : J\,\rangle$, where L_f, S_f, J_f are orbital, spin and total angular momenta of the residual ion, respectively, and ℓ and j are orbital and total angular momenta of the photoelectron.

The scheme of the process is depicted in Fig. 12.4. It should be noted that, while the discrete intermediate state can have either non-generate or degenerate HFS levels, the HFS of the final continuum state can be considered to be degenerate.

Such a scheme in which HFS effects take place only in the intermediate stage for the instantaneous and coherent excitation with long observation times allows us to represent its polarization as a product[3] of the resultant polarization of the electronic shell,

$$\rho_{k_1 q_1}(J_i;\,J_i') = \hat{J}_0^{-1}(-1)^{J_0+J_i+k_1+1}\,\hat{J}_i\,\hat{J}_i'\,\rho^{(\gamma)}_{k_1 q_1}\begin{Bmatrix} 1 & J_i & J_0 \\ J_i' & 1 & k_1 \end{Bmatrix} D_{J_0,J_i}\,D^*_{J_0,J_i'} \tag{12.5}$$

and the depolarization factor originating from the nuclear spin precession

$$\begin{aligned} h_k(I) = \mathscr{H}\frac{1}{\hat{I}^2}\sum_{FF'}\hat{F}^2\hat{F}'^2\begin{Bmatrix} F & F' & k \\ J_i' & J_i & I \end{Bmatrix}^2 \\ \times\int_{-\infty}^{\infty}\int_{-\infty}^{t_2} E_1(t_1)E_2(t_2)\,\exp[-i\omega_{FF'}(t_2-t_1) - \Gamma(t_2-t_1)]\,dt_1 dt_2\,, \end{aligned} \tag{12.6}$$

[3]The easiest way to obtain this is to consider the system in the initial state as a product of two subspaces, the electronic shell momentum and the nuclear spin $\hat{J}\bigotimes\hat{I}$, and then, couple them to the total angular momentum $\hat{F}$ only after the excitation.

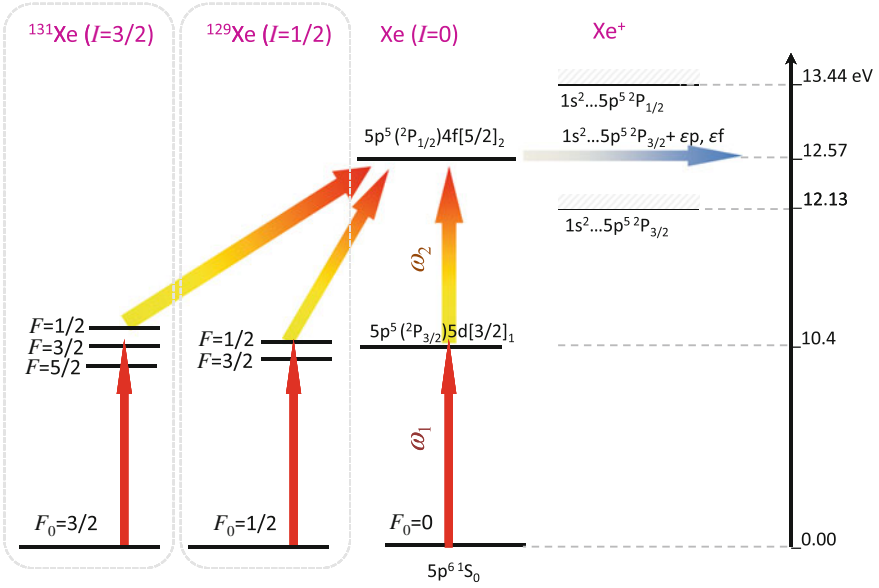

Fig. 12.4 Scheme of two-colour resonant ionization of xenon isotopes with different nuclear spin in the region of the Xe$^{**}(5p^5\,{}^2P_{1/2})4f\,[5/2]_2$ Rydberg autoionizing state

where the sum is taken over HFS levels $F,\ F'$; $E_1(t)$ and $E_2(t)$ are envelopes of the first (ω_1) and second (ω_2) laser fields, and the width Γ is supposed to be common for all HFS levels. In the reduced dipole matrix element, $D_{J_0 J_i} = \langle \alpha_i J_i \,||\, \hat{D} \,||\, \alpha_0 J_0 \rangle$, the initial (excited) state is characterized by the total angular momentum of the electronic shell J_0 (J_i) and a set of other quantum numbers α_0 (α_i); $\rho^{(\gamma)}_{k_1 q_1}$ is a statistical tensor of the photon (see Sect. 12.2.2). We have introduced the abbreviation $\hat{a} = \sqrt{2a+1}$ and the standard notations for nj-symbols. The depolarization factor (12.6), which includes also the depolarization induced by collisions ($\mathscr{H} \approx 1$), depends on the nuclear spin, atomic angular momentum, energy, time and splitting (see Sect. 12.2.3 for further discussion).

The photoelectron angular distribution in the two-step resonant ionization[4] can be cast into the form [5].

$$\frac{\mathrm{d}\sigma}{\mathrm{d}\Omega} = \frac{\pi\omega}{c} \sum_{\substack{kq k_1 q_1 \\ k_2 q_2}} h_{k_1}(I)\, B(k_1, k, k_2)\, \rho^{(\gamma)}_{k_2 q_2}\, \rho_{k_1 q_1}(J_i, J_i') \times (k_1 q_1, k_2 q_2 \,|\, kq)\, \frac{1}{\sqrt{4\pi}\,\hat{k}}\, Y_{kq}(\vartheta, \varphi)\,, \tag{12.7}$$

[4]The statistical tensor (12.5) has a dimension of probability per second, while the dimension of the two-photon cross section (12.7) is cm^2/s.

where c^{-1} is the fine-structure constant. The parameters $B(k_1, k, k_2)$ contain information about the dynamics of the electron emission, including the interference of direct and resonant ionization paths [17], and is given by:

$$B(k_1,k,k_2) = \hat{k}_1\hat{k}_2 \sum_{\substack{\ell\ell' jj' \\ JJ'}} (-1)^{J_f+J+k-1/2}\hat{\ell}\hat{\ell}'\hat{j}\hat{j}'\hat{J}\hat{J}'\big(\ell 0,\ell' 0\,|\,k0\big) \times \begin{Bmatrix} k & J & J' \\ J_f & L' & L \end{Bmatrix} \begin{Bmatrix} j & \ell & 1/2 \\ \ell' & j' & k \end{Bmatrix} \begin{Bmatrix} J_i & 1 & J \\ J_i' & 1 & J' \\ k_1 & k_2 & k \end{Bmatrix} \mathscr{D}_{\ell jJ}\mathscr{D}^*_{\ell' j' J'}\,. \quad (12.8)$$

where J is total angular momentum of the system after photoemission. The dynamical parameters (12.8)[5] satisfy the relationship $B(k_1,k,k_2) = (-1)^{J_i-J_i'+k_1+k_2+k}B^*(k_1, k, k_2)$. Discussion of the amplitudes $\mathscr{D}_{\ell jJ}$ of photoemission into a particular channel is given in Sect. 12.2.1.

12.2.1 Role of Autoionization

Assume that discrete and continuum configurations of atom are mixed by interaction V, which is usually the Coulomb interaction. The decay of the autoionizing state with total angular momentum of the electronic shell J_a and other quantum numbers α_a is then described by the reduced matrix elements ('decay amplitudes') $V_{\ell jJ} = \langle \alpha_f J_f \ell j J \,||\, \hat{V} \,||\, \alpha_a J_a\rangle$. The full autoionization width is given by $\Gamma_a = 2\pi \sum_{\ell jJ} |V_{\ell jJ}|^2$, provided only one final ionic state $\alpha_f J_f$ is possible. The interference between the direct and the resonant ionization paths in the region of an isolated autoionizing state may be taken into account by presenting the dipole matrix elements in (12.8) in the form [5, 32],

$$\mathscr{D}_{\ell jJ} = e^{i\delta_{\ell jJ}} \left(\frac{\sum_{\ell' j' J'} D_{\ell' j' J'} V_{\ell' j' J'}}{\sum_{\ell' j' J'} |V_{\ell' j' J'}|^2} V_{\ell jJ} \frac{q-i}{\epsilon+i} + D_{\ell jJ} \right), \quad (12.9)$$

where q is the Fano profile index [17], $\epsilon = 2(E - E_a)/\Gamma_a$ is the detuning from the resonance position E_a, $\delta_{\ell jJ}$ is the scattering phase in the corresponding ionization channel, and the reduced amplitudes of the direct ionization is denoted as $D_{\ell jJ} = \langle \alpha_f J_f \ell j J \,||\, \hat{D} \,||\, \alpha_i J_i\rangle$ (see (12.4) and (12.5) of [25]). The amplitude (12.9) turns into the reduced dipole direct ionization amplitude far from the resonance ($\epsilon \to \pm\infty$): $\mathscr{D}_{\ell jJ} \to e^{i\delta_{\ell jJ}} D_{\ell jJ}$.

[5] The first $6j$-symbol was missed in (6) of [26].

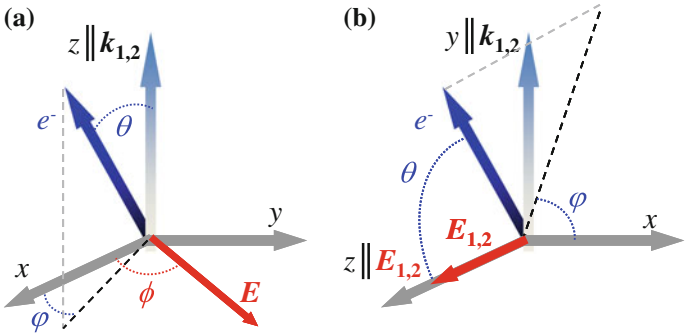

Fig. 12.5 The coordinate system for arbitrary polarization of two collinearly propagating field (**a**) and for particular case when both fields are linearly polarized in the same direction (**b**). Dashed black lines mark the projection of the direction of electron emission on the xy-plane

12.2.2 Statistical Tensors of Photon

We choose z-axis along the radiation beams $\boldsymbol{k}_{1,2}$, see Fig. 12.5a, the direction of the x-axis will be specified in the Sect. 12.3.1 (whether along synchrotron or laser polarization vector, $\boldsymbol{E}_1$ or $\boldsymbol{E}_2$, respectively). In this coordinate system a general form of the photon statistical tensors in the dipole approximation,[6] expressed via the Stocks parameters $p_1,\ p_2,\ p_3$ was presented, for example, in [6]:

$$\rho_{00}^{(\gamma)} = 1/\sqrt{3}\,,\quad \rho_{10}^{(\gamma)} = p_3/\sqrt{2}\,, \tag{12.10}$$

$$\rho_{20}^{(\gamma)} = 1/\sqrt{6}\,,\quad \rho_{2\pm2}^{(\gamma)} = -(p_1 \mp i p_2)/2\,. \tag{12.11}$$

For the radiation linearly polarized in the direction determined by the angle ϕ (see Fig. 12.5a), its statistical tensors with nonzero projection take the form $\rho_{2\pm2}^{(\gamma)} = -\exp(-2i\phi)/2$. There is one geometrically specified case when both fields are linearly polarized in the same direction. For this case it is convenient to choose the z-axis along the polarization vectors (see Fig. 12.5b). Then, only two statistical tensors are nonvanishing:

$$\rho_{00}^{(\gamma)} = 1/\sqrt{3}\,,\quad \rho_{20}^{(\gamma)} = -\sqrt{2/3}\,. \tag{12.12}$$

[6] Statistical tensors of photon in the dipole approximation are defined according to (12.2) for a particle with the angular momentum $J = 1$ having zero projection on the direction of the propagation.

12.2.3 Depolarization Factors

Suppose that all HFS levels are excited coherently and their decay does not affect internal motions in the nucleus. Assuming that fields are monochromatic with constant amplitudes and taking integrals in (12.6) one gets for the depolarization factor

$$h_k(I) = \frac{1}{\hat{I}^2} \sum_{FF'} \hat{F}^2 \hat{F}'^2 \begin{Bmatrix} F & F' & k \\ J_i' & J_i & I \end{Bmatrix}^2 \left(1 + \frac{\omega_{FF'}^2}{\Gamma^2}\right)^{-1} . \tag{12.13}$$

For the degenerate HFS ($\omega_{FF'} = 0$), the sum in (12.13) can be taken analytically with the result $h_k(I) = 1$. Thus, there is no depolarization for overlapping HFS levels. In the opposite limit, when the HFS levels are well separated ($\omega_{FF'} \gg \Gamma$) only diagonal terms with $F = F'$ survive.

The main term of hyperfine energy correction may be expressed as $A\,(F(F+1) - I(I+1) - J(J+1))\,/2$ [34], where A is the HFS coupling constant for the level under consideration. For our case $J_i = 1$ and nuclear spin $I = 1/2,\ 3/2$ the depolarization factors are

$$h_1(1/2) = \frac{7}{9} + \frac{2}{9} \cdot \frac{1}{1 + 2.25\alpha} \to 7/9\,, \tag{12.14}$$

$$h_2(1/2) = \frac{1}{3} + \frac{2}{3} \cdot \frac{1}{1 + 2.25\alpha} \to 1/3\,,$$

$$h_1(3/2) = \frac{19}{45} + \frac{5}{18} \cdot \frac{1}{1 + 2.25\alpha} + \frac{3}{10} \cdot \frac{1}{1 + 6.25\alpha} \to \frac{19}{45}\,, \tag{12.15}$$

$$h_2(3/2) = \frac{37}{150} + \frac{1}{30} \cdot \frac{1}{1 + 2.25\alpha} + \frac{3}{10} \cdot \frac{1}{1 + 16\alpha} + \frac{21}{50} \cdot \frac{1}{1 + 6.25\alpha} \to \frac{37}{150}\,.$$

We introduced the parameter $\alpha = (A/\Gamma)^2$. Limits in (12.14), (12.15) are indicated for the case when the energy splitting between the HFS levels are much larger than the width Γ ($\alpha \gg 1$). It is worth noting that these limits give lowest possible values for the depolarization produced by the HFS. Partial overlapping of the HFS levels reduces depolarization and increases the factors $h_k(I)$. For a larger nuclear spin the limiting values of $h_k(I)$ are lower and the depolarization is more efficient.

12.3 Observable Quantities

The experiments were performed at the vacuum ultraviolet variable polarization beam line DESIRS [41], the French synchrotron source, SOLEIL, whose scientific scope includes the study of photoionization dynamics and circular dichroism. For more experimental details see [26, 44], here we concentrate on theoretical analysis of the experimental results. As mentioned above, the natural mixture of xenon contains

Table 12.1 Natural abundance (%) of the xenon isotopes and their nuclear spin I

	^{124}Xe	^{126}Xe	^{128}Xe	^{129}Xe	^{130}Xe	^{131}Xe	^{132}Xe	^{134}Xe	^{136}Xe
I	0	0	0	1/2	0	3/2	0	0	0
	0.00095	0.00089	0.0191	0.264	0.0407	0.212	0.269	0.104	0.088

two valuable species of stable isotopes with non-zero spins, ^{129}Xe ($I = 1/2$) and ^{131}Xe ($I = 3/2$) (see Table 12.1).

Photoelectron angular distributions were measured in coincidence with a mass (nuclear isotope) selected ion in the following five different combinations of the polarizations of two collinearly propagating light beams: (i) two linearly polarized light beams having the same polarization direction, (ii) two linearly polarized beams whose polarization directions are perpendicular to each other, (iii) two left-handed circularly polarized light beams, (iv) two right-handed circularly polarized light beams, and (v) a left-handed circularly polarized light beam and a right-handed circularly polarized light beam. In addition, two dichroisms integrated over the angles of the electron emission, that is, integrated circular magnetic dichroism (CMD) and integrated linear dichroism (LD) were measured.

12.3.1 Linear and Circular Dichroism and Determination of Hyperfine Constant

When both of the fields are linearly polarized, we take $z \parallel \boldsymbol{E}_1$ and ϕ is the angle between $\boldsymbol{E}_1$ and $\boldsymbol{E}_2$. For the angle-integrated photionization cross section one can obtain from (12.7)–(12.8)

$$\sigma^{LL} = \frac{\pi\omega}{c}\left(\left[1 + h_2\frac{1+3\cos 2\phi}{20}\right]\sum_{\ell j}|\mathscr{D}_{\ell j J=2}|^2 + \left[1 - h_2\frac{1+3\cos 2\phi}{4}\right]\sum_{\ell j}|\mathscr{D}_{\ell j J=1}|^2 + \right.$$
$$\left. + \left[1 + h_2\frac{1+3\cos 2\phi}{2}\right]\sum_{\ell j}|\mathscr{D}_{\ell j J=0}|^2\right). \tag{12.16}$$

Linear dichroism is the difference in the cross-sections measured for parallel ($\phi = 0$) and perpendicular ($\phi = 90°$) polarization directions. One obtains from (12.16):

$$\mathrm{LD} = \frac{\sigma^{\parallel} - \sigma^{\perp}}{\sigma^{\parallel} + \sigma^{\perp}} \tag{12.17}$$
$$= 3h_2\frac{\sum_{\ell j}\left(\frac{1}{20}|\mathscr{D}_{\ell j J=2}|^2 - \frac{1}{4}|\mathscr{D}_{\ell j J=1}|^2 + \frac{1}{2}|\mathscr{D}_{\ell j J=0}|^2\right)}{\sum_{\ell j}\left((1+\frac{h_2}{20})|\mathscr{D}_{\ell j J=2}|^2 + (1-\frac{h_2}{4})|\mathscr{D}_{\ell j J=1}|^2 + (1+\frac{h_2}{2})|\mathscr{D}_{\ell j J=0}|^2\right)}.$$

When both fields are circularly polarized with equal (++) or opposite (+−) helicities, the angle-integrated cross section is

$$\sigma^{+\pm} = \frac{\pi\omega}{c}\left(\left[1 \pm \frac{3}{4}h_1 + \frac{h_2}{20}\right]\sum_{\ell j}|\mathscr{D}_{\ell j J=2}|^2 + \left[1 \mp \frac{3}{4}h_1 - \frac{h_2}{4}\right]\sum_{\ell j}|\mathscr{D}_{\ell j J=1}|^2 + \right.$$
$$\left. + \left[1 \mp \frac{3}{2}h_1 + \frac{h_2}{2}\right]\sum_{\ell j}|\mathscr{D}_{\ell j J=0}|^2\right). \tag{12.18}$$

The circular magnetic dichroism follows from (12.18):

$$\mathrm{CMD} = \frac{\sigma^{++} - \sigma^{+-}}{\sigma^{++} + \sigma^{+-}} \tag{12.19}$$
$$= 3h_1 \frac{\sum_{\ell j}(|\mathscr{D}_{\ell j J=2}|^2 + |\mathscr{D}_{\ell j J=1}|^2 + 2|\mathscr{D}_{\ell j J=0}|^2)}{4\sum_{\ell j}\left((1+\frac{h_2}{20})|\mathscr{D}_{\ell j J=2}|^2 + (1-\frac{h_2}{4})|\mathscr{D}_{\ell j J=1}|^2 + (1+\frac{h_2}{2})|\mathscr{D}_{\ell j J=0}|^2\right)}.$$

Equations (12.17) and (12.19) allow to set limits for both of the two types of dichroism. As a rule, autoionization significantly amplifies the channels with $J = J_a$. In our case of resonant ionization in the vicinity of the autoionizing state $\mathrm{Xe}^{**}(5p^5\,{}^2P_{1/2})4f[5/2]_2$, channels with $J = 2$ should be enhanced. Neglecting channels with $J = 0, 1$, we obtain from (12.17) and (12.19),

$$\mathrm{LD} = \frac{3\,h_2}{20 + h_2}, \tag{12.20}$$

$$\mathrm{CMD} = \frac{15\,h_1}{20 + h_2}. \tag{12.21}$$

Measured values of dichroism are expected to be lower than defined by (12.20), (12.21), because resonant approximation is not well satisfied on tails of the resonance profile. Nevertheless, the resonance $\mathrm{Xe}^{**}(5p^5\,({}^2P_{1/2})4f[5/2]_2$ chosen here is quite strong with q-index from 4 to 10 in different models [26, 50]. Thus we believe that comparison of the measured dichroism with the limit values is useful. It is seen from Table 12.2 that the agreement for CMD is surprisingly good for isotopes with $I = 0,\ 1/2$. As expected from (12.20), (12.21), and (12.14), (12.15), the experimental values of CMD is much larger than of LD, therefore, meaningful conclusions may be drawn only from the CMD values.

The accurate consideration of the weak channels with $J = 0,\ 1$ performed in multiconfiguration Hartree-Fock approximation [26] gives only a little lower values than in the resonance model. The agreement of the measured dichroism with the algebraic expectation for ^{129}Xe ($I = 1/2$) isotope means that the HFS levels for this isotope are well separated and their depolarization are the strongest.

Surprisingly, the measured dichroism for ^{131}Xe ($I = 3/2$) isotope is noticeably above the expected value. This means that the HFS levels overlap, decreasing the

Table 12.2 Measured and calculated linear and circular dichroism. Numbers in parenthesis give experimental uncertainties

Experiment				Theory		
I	0	1/2	3/2	0	1/2	3/2
LD	0.11 (2)	0.03 (3)	0.04 (3)	$\frac{1}{7} \approx 0.14$	$\frac{3}{61} \approx 0.05$	$\frac{111}{3037} \approx 0.037$
CMD	0.67 (2)	0.54 (4)	0.43 (4)	$\frac{5}{7} \approx 0.71$	$\frac{35}{61} \approx 0.57$	$\frac{950}{3037} \approx 0.31$

effect of depolarization. Based on this observation, we proposed a method to determine the hyperfine structure constant A for partly overlapping HFS levels, which cannot be resolved spectroscopically. By substituting (12.15) into (12.21) and by using the measured CMD, one can obtain a simple equation for α. Our estimate gives $A/\Gamma = 0.85 \pm 0.14$ and the depolarization factors, $h_1(3/2) = 0.58 \pm 0.04$ and $h_2(3/2) = 0.35 \pm 0.04$.

12.3.2 Photoelectron Angular Distribution

In this section we consider three possible geometries: both fields are linearly polarized in the same direction, both fields are circularly polarized with equal helicities and with opposite helicities. The last two cases imply collinearly propagating fields. For these polarization sets the photoelectron angular distribution is axially symmetric with respect to the polarization vector or propagation direction and, in each case, can be determined by two corresponding dimensionless angular anisotropy parameters, β_2^{ν} and β_4^{ν} as:

$$\frac{\mathrm{d}\sigma}{\mathrm{d}\Omega} = \frac{\sigma^{\nu}}{4\pi}\left(1 + \beta_2^{\nu} P_2(\cos\theta) + \beta_4^{\nu} P_4(\cos\theta)\right), \tag{12.22}$$

index $^{\nu} = lin, ++, +-$ indicates cases when both of the fields are either linearly polarized in one direction, or circularly polarized with equal or opposite helicities; $P_n(x)$ is the Legendre polynomial and θ measured from the symmetry axis. The second-rank polynomial produces an 'eight'-like form of the photoelectron angular distribution, while the fourth-rank polynomial is responsible for its 'butterfly'-like component. The depolarization leads to the reduction of the value of β_4.

For convenience, we introduce modified dynamical parameters instead of (12.8) as follows: $\mathscr{B}_{000} = \frac{1}{3}B(0,0,0)$, $\mathscr{B}_{202} = \frac{\sqrt{5}}{6}B(2,0,2)$, $\mathscr{B}_{022} = \frac{\sqrt{10}}{12}B(0,2,2)$, $\mathscr{B}_{220} = \frac{\sqrt{10}}{12}B(2,2,0)$, $\mathscr{B}_{222} = \frac{5\sqrt{14}}{42}B(2,2,2)$, $\mathscr{B}_{242} = \frac{\sqrt{70}}{672}B(2,4,2)$, $\mathscr{B}_{122} = \frac{\sqrt{30}}{12}B(1,2,2)$, $\mathscr{B}_{221} = \frac{\sqrt{30}}{12}B(2,2,1)$, $\mathscr{B}_{101} = \frac{\sqrt{3}}{2}B(1,0,1)$, $\mathscr{B}_{121} = \frac{\sqrt{6}}{2}B(1,2,1)$. Then, the angular anisotropy parameters can be presented in the following forms:

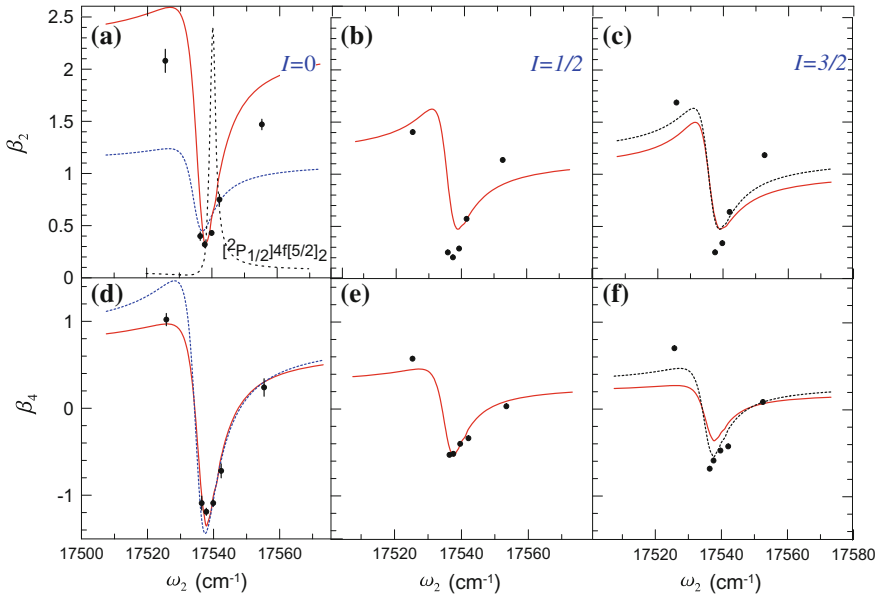

Fig. 12.6 Angular anisotropy parameters as function of second (ionizing) laser energy measured in coincidence with nuclear isotopes of the residual ion. Both fields are linearly polarized in the same direction. Multiconfiguration Hartree-Fock results (red solid) are obtained by assuming that HFS states for the isotopes with nonzero spin $I = 1/2, 3/2$ are well isolated ($\alpha \gg 1$). Blue dashed curves in the panels $I = 3/2$ present results with α obtained in Sect. 12.3.1. The dashed curves in panels (**a**) and (**b**) show the results obtained when only the resonant channels with $J = 2$ are included. The profile of the $Xe^{**}(5p^5\,{}^2P_{1/2})4f[5/2]_2$ resonance in the angle-integrated cross section σ is shown in panel (**a**) for comparison (black dotted line)

$$\beta_2^{lin} = -4\,\frac{h_2(\mathscr{B}_{220}+\mathscr{B}_{022})+\mathscr{B}_{222}}{\mathscr{B}_{000}+4h_2\mathscr{B}_{202}}\,,$$
$$\beta_4^{lin} = \frac{192\,h_2\mathscr{B}_{242}}{\mathscr{B}_{000}+4h_2\mathscr{B}_{202}}\,, \tag{12.23}$$

$$\beta_2^{+\pm} = \frac{2\mathscr{B}_{022}+h_2(2\mathscr{B}_{220}-\mathscr{B}_{222})\pm h_1\mathscr{B}_{121}}{\mathscr{B}_{000}\mp h_1\mathscr{B}_{101}+h_2\mathscr{B}_{202}}\,,$$
$$\beta_4^{+\pm} = \frac{48\,h_2\mathscr{B}_{242}}{\mathscr{B}_{000}\mp h_1\mathscr{B}_{101}+h_2\mathscr{B}_{202}}\,. \tag{12.24}$$

Figures 12.6 and 12.7 present the asymmetry parameters (12.23) and (12.24) in the region around the $Xe^{**}(5p^5\,{}^2P_{1/2})4f[5/2]_2$ resonance for isotopes with different nuclear spins. The parameter β_4^{ν} would vanish for an unpolarized intermediate $Xe^*(5p^5\,{}^2P_{3/2})5d[3/2]_1$ state. The high values reached by β_4^{ν} indicate high anisotropy of this state.

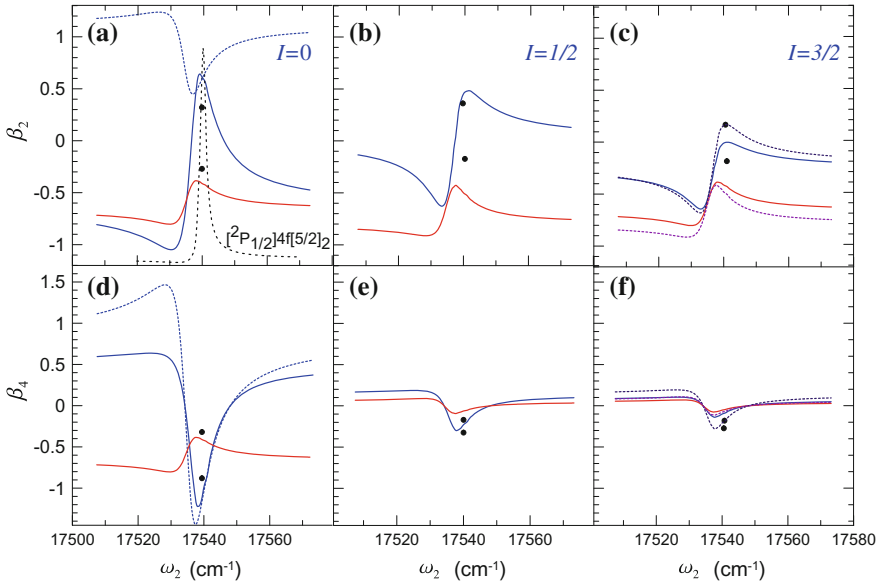

Fig. 12.7 The same as in Fig. 12.6, for circularly polarized fields. Red curves mark equal helicities (++), blue curves mark opposite helicities (+−)

In the panels (a) and (d) of Figs. 12.6 and 12.7 we present angular anisotropy parameters calculated in the complete model [26] and in the model when only the resonant channels with $J = 2$ ("resonant model") are included, with $h_1 = h_2 = 1$. In the panels (a) and (d) of the same figures, the curves are closer in the vicinity of the resonance, but deviate from each other significantly at tails of the resonance. For opposite helicities, β_2 in the resonant and the complete model even inverts the shape (blue dashed and solid curves in Fig. 12.7). For equal helicities the weak channels with $J = 0, 1$ are not excited for the isotope with $I = 0$ (i.e. without the depolarization) due to the selection rules for the magnetic quantum number. Therefore only $\beta_{2,4}^{+-}$ are changed by inclusion of the weak channels and their influence is crucial (panels (a) and (d) of Figs. 12.6 and 12.7). The resonance behavior of the β_2 parameter changes completely from the window-type to the resonance-type.

The calculation of the electronic structure does not differ for the different isotopes and the results for the anisotropy parameters for the isotopes should be automatically consistent once the depolarization factors due to the coupling between the electronic and nuclear angular momenta are properly included (see Sects. 12.2.3, 12.3.1). As can be seen in the panels (c)–(f) of Figs. 12.6 and 12.7, one do may use the same atomic spectroscopic model for all the isotopes.

For the ^{131}Xe ($I = 3/2$) isotope, the depolarization coefficients found above from the analysis of the CMD data (see Sect. 12.3.1), lead to slightly better agreement between theory and experiment than when the assumption of the separated HFS levels (panels (e) and (f) of Figs. 12.6 and 12.7) is made. Note that the profiles for

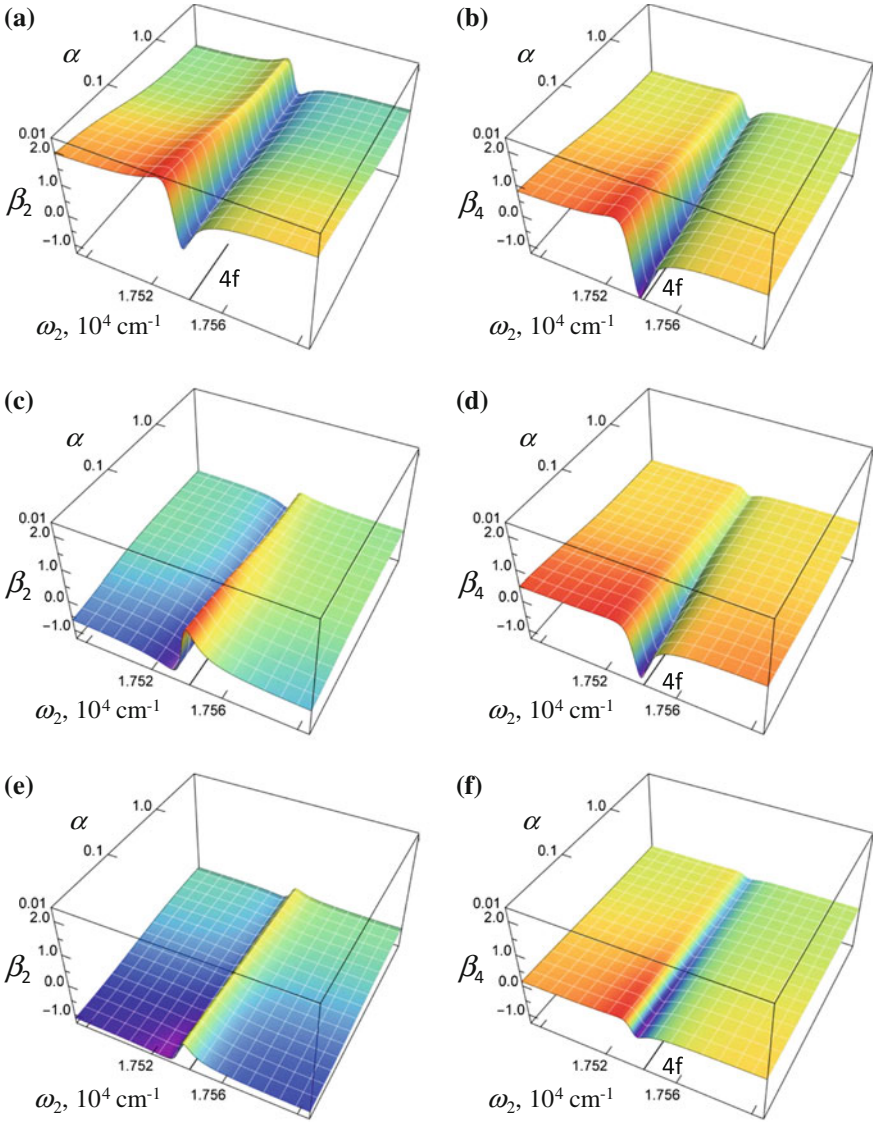

Fig. 12.8 Calculations for the isotope ^{131}Xe ($I = 3/2$): Angular anisotropy parameters as function of second (ionizing) laser energy and the depolarization factor α when both fields are linearly polarized in the same direction (**a**, **b**); one field is right and other field is left polarized (**c**, **d**) and both fields are right polarized (**e**, **f**). The position of the $Xe^{**}(5p^5\,^2P_{1/2})4f\,[5/2]_2$ state is indicated on the ω_2 axis by a long tick, marked as 4f

$\beta_{2,4}^{\nu}$ for all isotopes are equally broadened and shifted with respect to the profile of the resonance in the angle-integrated cross section in accordance with the scaling theorem [24].

To further illustrate the sensitivity of the asymmetry parameters to the hyperfine interaction, Fig. 12.8 presents the resonance profiles of β_2^{ν} and β_4^{ν} as function of laser energy and the parameter α for the isotope with $I = 3/2$. As we have mentioned in Sect. 12.2.3, even for infinite α the HFS depolarization is restricted, therefore, β_k does not change with further increasing α. From the limit value of $h_2(3/2)$ (see (12.15)) one may expect that β_4^{ν} decreases 4 times because of depolarization (Fig. 12.8b, d, f), but does not vanish. Therefore only collisional depolarization may completely demolish β_4. Besides decreasing of high-rank anisotropy parameters, the depolarization also opens some forbidden channels. In the case under consideration, these are channels $\mathrm{Xe}^+(5p^{5\,2}P_{3/2}\varepsilon\ell : J = 1)$ for linearly polarized fields and $\mathrm{Xe}^+(5p^{5\,2}P_{3/2}\varepsilon\ell : J = 0, 1)$ for circularly polarized light beams with equal helicity. The values of β_2^{ν} at the tails of the resonance are determined by a complicated interplay of the contributing channels (Fig. 12.8a, c, e).

12.4 Future Directions

Recent rapid progress in generation of VUV and X-Ray light pulses as well as their detection introduced an evolution in experimental studies on the effects of the hyperfine interactions from alkali and alkali earth atoms to noble gases. Even the investigation of positively charged ions became possible through sequential ionization (see chapter [25] in this book). The free-electron laser facilities, which are currently in operation, as well as those to be in operation in the near future can generate pulses with good longitudinal coherence, high brightness and short duration, with which we can investigate a variety of phenomena strongly affected by HFS by time- and angular-resolved photoelectron spectroscopy in the high-frequency domain. For example, by controlling and monitoring properties of the high-frequency radiation, we can investigate the effect of hyperfine interactions in the decay process of inner-shell vacancies.

Acknowledgements The authors highly appreciate the team of experimentalists, D. Cubaynes, G. A. Garcia, M. Meyer, L. Nahon and P. O'Keeffe, whose inspiration measurements initiated our theoretical study. We are grateful to kind hospitality of the French synchrotron SOLEIL and the European XFEL. EVG acknowledges financial support from the Basis foundation via the Junior Leader program.

References

1. E.B. Aleksandrov, V.N. Kulyasov, Sov. Phys. JETP **28**, 396–400 (1969)
2. E.B. Aleksandrov, Sov. Phys. JETP **29**, 846–848 (1969)
3. E.B. Aleksandrov, V.P. Kozlov, V.N. Kulyasov, Sov. Phys. JETP **39**, 620–626 (1974)
4. S. Aloïse, P. O'Keeffe, D. Cubaynes, M. Meyer, A.N. Grum-Grzhimailo, Phys. Rev. Lett. **94**, 223002(1)–223002(4) (2005)
5. S. Baier, A.N. Grum-Grzhimailo, N.M. Kabachnik, J. Phys. B **27**, 3363–3388 (1994)
6. V.V. Balashov, A.N. Grum-Grzhimailo, N.M. Kabachnik, *Polarization and Correlation Phenomena in Atomic Collisions. A Practical Theory Course* (Kluwer Plenum, New York, 2000)
7. B.B. Birkett, J.-P. Briand, P. Charles et al., Phys. Rev. A **47**, R2454–R2457 (1993)
8. K. Blum, *Density Matrix Theory and Applications*, 2nd edn (Plenum, New York, 1996)
9. M. Born, J.R. Oppenheimer, Annalen der Physik **389**, 457–484 (1927)
10. T. Brage, P.G. Judge, C.R. Proffitt, Phys. Rev. Lett. **89**, 281101(1)–281101(4) (2002)
11. A.W. Carr, M. Saffman, Phys. Rev. Lett. **117**, 150801(1)–150801(6) (2016)
12. R.-L. Chien, O.C. Mullins, R.S. Berry, Phys. Rev. A **28**, 2678–2084 (1983)
13. L.E. Cuéllar, C.S. Feigerle, H.S. Carman Jr., R.N. Compton, Phys. Rev. A **45**, 6437–6440 (1991)
14. B. Denne, S. Huldt, J. Pihl, R. Hallin, Phys. Scr. **22**, 45–48 (1980)
15. J.A. Duncanson Jr., M.P. Strand, A. Lindgård, R.S. Berry, Phys. Rev. Lett. **37**, 987–990 (1976)
16. L. Essen, J.V.L. Parry, Nature **176**, 280–282 (1955)
17. U. Fano, Phys. Rev. **124**, 1866–1978 (1961)
18. U. Fano, J.H. Macek, Phys. Rev. **45**, 553–573 (1973)
19. P.M. Farrell, W.R. MacGillivray, M.C. Standage, Phys. Rev. A **44**, 1828–1835 (1991)
20. C.S. Feigerle, R.N. Compton, L.E. Cuéllar, N.A. Cherepkov, L.V. Chernysheva, Phys. Rev. A **53**, 4183–4189 (1996)
21. V.V. Flambaum, V.A. Dzuba, A. Derevianko, Phys. Rev. Lett. **101**, 220801(1)–220801(4) (2008)
22. R. Forbes, V. Makhija, A. Stolow, I. Wilkinson, P. Hocketty, R. Lausten, Phys. Rev. A **97**, 063417(1)–063417(11) (2018)
23. M. Göppert-Mayer, Phys. Rev. **78**, 16–21 (1950)
24. A.N. Grum-Grzhimailo, S. Fritzsche, P. O'Keeffe, M. Meyer, J. Phys. B **38**, 2545–2553 (2005)
25. A.N. Grum-Grzhimailo, E.V. Gryzlova, Chapter *New Trends in Complete Experiment on Atomic Photoionization* (in this book)
26. E.V. Gryzlova, P. O'Keeffe, D. Cubaynes, G.A. Garcia, L. Nahon, A.N. Grum-Grzhimailo, M. Meyer, New J. Phys. **17**, 043054(1)–043054(15) (2015)
27. E. Hack, J.R. Huber, Int. Rev. Phys. Chem. **10**, 287–317 (1991)
28. T. Hadeishi, W.A. Nierenberg, Phys. Rev. Lett. **14**, 891–892 (1965)
29. S. Haroche, J.A. Paisner, A.L. Schawlow, Phys. Rev. Lett. **30**, 948–951 (1973)
30. J.R. Henderson, P. Beiersdorfer, C.L. Bennett et al., Phys. Rev. Lett. **65**, 705–708 (1990)
31. D. Huff, W.V. Houston, Phys. Rev. **36**, 842–846 (1930)
32. N.M. Kabachnik, I.P. Sazhina, J. Phys. B **9**, 1681–1697 (1976)
33. A. Kupliauskiene, N. Rakštikas, V. Tutlys, J. Phys. B **34**, 1783–1803 (2001)
34. L.D. Landau, E.M. Lifshitz, *Quantum Mechanics: Non-Relativistic Theory, 3rd edn* (Pergamon, London, 1977)
35. R. Luypaert, J. Van Craen, J. Phys. B **10**, 3627–3636 (1977)
36. J.J. McClelland, M.H. Kelley, Phys. Rev. A **31**, 3704–3710 (1985)
37. M. Meyer, B. Müller, A. Nunnemann, Th. Prescher, E.V. Raven, M. Richter, M. Schmidt, B. Sonntag, P. Zimmermann, Phys. Rev. Lett. **59**, 2963–2966 (1987)
38. M. Meyer, M. Gisselbrecht, A. Marquette, C. Delisle, M. Larzillière, I.D. Petrov, N.V. Demekhina, V.L. Sukhorukov, J. Phys. B **38**, 285–295 (2005)
39. S. Mrozowski, Phys. Rev. **57**, 207–211 (1940)
40. O.C. Mullins, R.-L. Chien, J.E. Hunter III, J.S. Keller, R.S. Berry, Phys. Rev. A **31**, 321–328 (1985)

41. L. Nahon, N. de Oliveira, G.A. Garcia, J.-F. Gil, B. Pilette, O. Marcouillé, B. Lagarde, F. Polack, J. Synchrotron Radiat. **19**, 508–520 (2012)
42. D.E. Nikonov, U.W. Rathe, M.O. Scully, S.-Y. Zhu, E.S. Fry, X. Li, G.G. Padmabandu, M. Fleischhauer, Quantum Opt. **6**, 245–260 (1994)
43. P. O'Keeffe, S. Aloïse, S. Fritzsche, B. Lohmann, U. Kleiman, M. Meyer, A.N. Grum-Grzhimailo, Phys. Rev. A **70**, 012705(1)–012705(14) (2004)
44. P. O'Keeffe, E.V. Gryzlova, D. Cubaynes, G.A. Garcia, L. Nahon, A.N. Grum-Grzhimailo, M. Meyer, Phys. Rev. Lett. **111**, 243002(1)–243002(5) (2013)
45. K.L. Reid, S.P. Duxon, M. Towrie, Chem. Phys. Lett. **228**, 351–356 (1994)
46. N. Saquet, D.M.P. Holland, S.T. Pratt, D. Cubaynes, X. Tang, G.A. Garcia, L. Nahon, K.L. Reid, Phys. Rev. A **93**, 033419(1)–033419(11) (2016)
47. A.L. Schawlow, C.H. Townes, Phys. Rev. **112**, 1940–1949 (1958)
48. J.H. Scofield, J. Nilsen, Phys. Rev. A **49**, 2381–2388 (1994)
49. A. Siegel, J. Ganz, W. Bußert, H. Hotop, J. Phys. B **16**, 2945–2959 (1983)
50. V. Sukhorukov, I. Petrov, M. Schäfer, F. Merkt, M.-W. Ruf, H. Hotop, J. Phys. B **45**, 092001(1)–092001(43) (2012)
51. J.R. Tolsma, D.J. Haxton, C.H. Greene, R. Yamazaki, D.S. Elliott, Phys. Rev. A **80**, 033401(1)–033401(9) (2009)
52. E. Träbert, P. Beiersdorfer, G.V. Brown, Phys. Rev. Lett. **98**, 263001(1)–263001(4) (2007)
53. W.A. van Wijngaarden, J. Sagle, J. Phys. B **24**, 897–903 (1991)
54. F. Wuilleumier, M. Meyer, J. Phys. B **39**, R425–R477 (2006)
55. R.P. Wood, C.H. Greene, D. Armstrong, Phys. Rev. A **47**, 229–235 (1993)
56. Z.W. Wu, A. Surzhykov, S. Fritzsche, Phys. Rev. A **89**, 022513(1)–022513(7) (2014)
57. H. Xu, E. Lötstedt, T. Ando, A. Iwasaki, K. Yamanouchi, Phys. Rev. A **96**, (R)041401(1)–041401(6) (2017)
58. J. von Zanthier, T. Becker, M. Eichenseer et al., Opt. Lett. **25**, 1729–1731 (2000)